

Flow-Directed Block Copolymer Micelle Morphologies via Microfluidic Self-Assembly

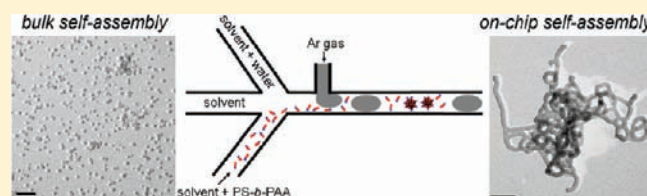
Chih-Wei Wang,[†] David Sinton,[‡] and Matthew G. Moffitt^{*,†}

[†]Department of Chemistry, University of Victoria, P.O. Box 3065, Victoria, BC, Canada V8W 3V6

[‡]Department of Mechanical and Industrial Engineering, University of Toronto, 5 King's College Road, Toronto, ON, Canada, M5S 3G8

S Supporting Information

ABSTRACT: The self-assembly of amphiphilic block copolymers in a gas–liquid microfluidic reactor produces variable, flow-directed micellar morphologies entirely different from off-chip equilibrium structures. A polystyrene-*block*-poly(acrylic acid) copolymer, which forms exclusively spheres off-chip, generates kinetic cylinders, Y-junctions, bilayers, and networks by a mechanism of collision–coalescence enabled by strong and localized on-chip shear fields. Variation in the size and relative amount of flow-directed nanostructures is achieved by changing the water content and flow rate. These results demonstrate on-chip processing routes to specific functional colloidal nanostructures.



INTRODUCTION

The solution self-assembly of amphiphilic block copolymers into colloidal nanostructures, termed block copolymer micelles, has spurred extensive fundamental and applied research in recent years.^{1–20} Of particular interest is the plethora of diverse micelle morphologies, including spheres, cylinders, and vesicles, that can spontaneously form in such systems, as a result of the exquisite and complex interplay of thermodynamic forces. A central focus of work in this area has been the understanding and control of these varied morphologies, because the size and shape of micellar structures will profoundly influence their effectiveness for specific applications, including drug delivery,^{21,22} sensing,²³ and medical imaging.^{24–26} Under equilibrium conditions, the morphologies of block copolymer micelles are governed by a fine balance of interfacial tension, chain stretching within the micelle core, and repulsion among solubilized coronal chains.^{1,2,5,7,8,10} However, along with such thermodynamic factors, kinetic effects arising from a combination of slow chain dynamics and high interfacial tension can also contribute significantly to the products of self-assembly, often leading to structurally complex and kinetically stable morphologies that are not globally equilibrated.^{5,10,13,14}

Conventional experimental control of block copolymer morphologies involves variation in chemical parameters that are known to directly influence intermolecular interactions (e.g., block copolymer composition,^{1,2} choice of solvent,⁸ polymer concentration,¹¹ pH, and ionic strength⁴). In contrast to this bottom-up approach, the top-down control of block copolymer morphologies through templates or external force fields (e.g., shear and magnetic and electric fields) opens the door to engineering micellar structures under a given set of chemical conditions by “dialing in” specific processing parameters. Although such directed assembly has been widely applied in block copolymer thin films using chemically and topologically defined

patterned substrates,^{27–32} there are very few examples of top-down morphological control in block copolymer colloids.^{33,34} In one example, Wu and co-workers extruded a block copolymer colloid through a nanoporous template to induce a sphere-to-cylinder micelle transition, with the resulting cylinders reverting back to spheres upon standing for several hours.³³ More recently, work from the Winnik group reported that block copolymer spherical micelles decorated with CdSe quantum dots could be converted to a wormlike network by rapid magnetic stirring, whereas similar stirring conditions yielded only spheres in the absence of quantum dots.³⁴

Microfluidic reactors have been studied as environments for the self-assembly of polymers^{35–43} and other molecular building blocks,^{44–46} because the associated nanoscale volumes and laminar flow enable fine-tuning of local concentrations of reagents, mixing rates, and shear forces. We recently applied a gas–liquid multiphase microfluidic reactor, in which compartmentalized liquid plugs are segmented by a regular stream of gas bubbles, in order to form spherical colloidal aggregates of polymer-coated quantum dots.^{41,42} In that work, we demonstrated that flow-variable high shear regions in the corners of the liquid plugs strongly influenced particle sizes via competing mechanisms of coalescence and particle break-up.⁴² In the present paper, we demonstrate that the solution self-assembly of amphiphilic block copolymers in a similar multiphase reactor leads to flow-variable micelle morphologies that are different from equilibrium structures produced by off-chip self-assembly under identical chemical conditions. The resulting shear-induced nanostructures are kinetically controlled by the on-chip flow environment but are stabilized by kinetic trapping after transfer from the reactor into aqueous environments. This approach

Received: July 19, 2011

Published: October 12, 2011

provides a convenient top-down handle on block copolymer morphologies through variation of microfluidic flow parameters, enabling facile processing control of colloidal nanostructures.

EXPERIMENTAL SECTION

Materials. The polystyrene-*block*-poly(acrylic acid) sample used in this study, PS(665)-*b*-PAA(68), was synthesized via anionic polymerization of the associated polystyrene-*block*-poly(*tert*-butyl acrylate) block copolymer, followed by hydrolysis of the ester block;^{47,48} numbers in parentheses refer to number-average degrees of polymerization of each block. Dimethylformamide (DMF) (Aldrich, 99.9+%, HPLC grade, H₂O < 0.03%) and 1,4-dioxane Aldrich, 99.0%, reagent grade, H₂O < 0.05% were used as received without further purification.

Critical Water Content Determination. In order to accurately determine the critical water content (*cwc*) of PS(665)-*b*-PAA(68) for the polymer concentration and solvent mixture applied in this study, static light scattering measurements were carried out. Light scattering experiments were performed on a Brookhaven Instruments photon correlation spectrometer equipped with a BI-200SM goniometer, a BI-9000AT digital autocorrelator, and a Melles Griot He–Ne Laser (632.8 nm) with a maximum power output of 75 mW. First, a stock solution was prepared by adding 75/25 (w/w) DMF/dioxane solvent mixture to a copolymer concentration of 0.66 wt %. The stock solution was then filtered through a Teflon syringe membrane filter with a nominal pore size of 0.45 μm (National Scientific Company) into precleaned scintillation vials. Next, the stock solution was diluted with 75/25 (w/w) DMF/dioxane solvent mixture filtered through two Teflon syringe filters with nominal pore size of 0.20 μm (National Scientific Company) connected in series to give a polymer concentration of 0.33 wt %. Deionized water was next added dropwise to ~ 6 g of the solution in successive 0.02–0.05 g quantities via a microsyringe equipped with a membrane filter (Life Sciences) with nominal pore size of 0.20 μm . After each addition of water, the solution was agitated with a vortexer to aid mixing. The scattered light intensity was recorded 15 min after vortexing to allow the solution to equilibrate. All measurements were carried out at a scattering angle of 90° and a temperature of 23 °C. The *cwc* thus obtained (Figure S1, Supporting Information) was 3.2 \pm 0.1 wt %.

Off-Chip Micelle Preparation. Morphologies formed on-chip under different chemical and flow conditions were compared to off-chip control experiments in which block copolymer micelles were prepared in the following manner. To three vials, each containing ~ 5 mL of 0.33 wt % PS(665)-*b*-PAA(68) in 75/25 (w/w) DMF/dioxane, deionized water was added dropwise at a rate of 20 μL every 10 s with moderate magnetic stirring (600 rpm) until the various target water concentrations were reached (4.2, 5.2, and 7.2 wt %). The resulting micelles were then allowed to equilibrate for 2 weeks without stirring, followed by kinetic trapping via transfer into ~ 50 mL deionized water. The colloidal dispersions were finally dialyzed against deionized water to remove residual organic solvent.

In addition, to compare the effects of off-chip stirring-induced shear with the effects of on-chip shear, we prepared micelles at 5.2 wt % water in a manner similar to that described above, except for the following differences. Once the target water concentration was reached, the micelles were stirred rapidly at 1200 rpm for a period of time equivalent to the on-chip residence time at low flow rate (280 s), followed by immediate kinetic trapping into excess deionized water and dialysis. In Figure S2, Supporting Information, this additional off-chip control experiment is referred to as “off-chip (rapid stirring)”.

Microfluidic Chip Fabrication. Negative masters were fabricated on high-quality silicon wafers (Silicon Quest International, Santa Clara, CA) using a negative photoresist, SU-8 100 (Microchem Inc.). Prior to use, new silicon wafers were heated on a hot plate to at 200 °C for 20 min

to remove all moisture. SU-8 films, 150 μm thick, were spin-coated onto the silicon wafers and then heated to 95 °C for 60 min to remove residual SU-8 solvent. A photomask was placed over the film, and the device was exposed to UV light for 180 s. After additional heating at 95 °C for 20 min, the device was submerged in SU-8 developer (Microchem) until all unexposed photoresist was removed. The reactor has a set channel depth of 150 μm and consists of a sinusoidal mixing channel 100 μm wide and 100 mm in length and a sinusoidal processing channel 200 μm wide and 740 mm in length.

For further stabilization of the bubble generation process, external resistor chips were employed in series between the Ar gas tank and the microfluidic chip. These resistors were 1000 mm long, 400 μm wide, and 150 μm deep. In operation, these high pressure drop resistors serve to efficiently dampen the pressure fluctuations caused by the Ar gas tank and the bubble generation process itself. The resistors were designed in a way that the total pressure drop in the resistors was at least 1 order of magnitude higher than the pressure drop in the reaction channel.

Microfluidic chips were fabricated from poly(dimethylsiloxane) (PDMS) using a SYLGARD 184 silicon elastomer kit (Dow Corning, Midland, MI) with an elastomer base-to-curing agent ratio of 10:1. The elastomer and curing agent were mixed together and degassed in a vacuum chamber. The degassed PDMS was poured onto the negative master in a Petri dish and then degassed again until all remaining air bubbles in the PDMS were removed. The PDMS was then heated at 85 °C until cured (~ 50 min). The microfluidic chips were peeled off the master, and holes were punched through its reservoirs to allow for the insertion of tubing. A thin PDMS film was formed on a glass slide by spin-coating and was permanently bonded to the base of the microfluidic reactor after both components were exposed to oxygen plasma for 30 s.

Flow Delivery and Control. Pressure-driven flow of liquids to the inlets of the reactors was provided using 250 μL gastight syringes (Hamilton, Reno, NV) mounted on syringe pumps (Harvard Apparatus, Holliston, MA). The microchip was connected to the syringes with 1/16th inch (OD) Teflon tubing (Scientific Products and Equipment, ON). Gas pressure was controlled by the Ar tank regulator as well as a downstream regulator for fine adjustments (Johnson Controls Inc.). For gas flow, connections were joined using Teflon tubing of 1/16 in. (OD) and 100 μm (ID) (Upchurch Scientific, Oak Harbor, WA). The liquid flow rate (Q_{liq}) was programmed via the syringe pumps, and the gas flow rate (Q_{gas}) was varied by tuning the pressure regulator. Due to the compressible nature of the gas and the high gas/liquid interfacial tension, discrepancies arise between the nominal (programmed) and actual values of Q_{gas} , $Q_{\text{gas}}/Q_{\text{liq}}$, and the total flow rate (Q_{total} , also denoted as Q for simplicity). Therefore, actual gas flow rates were calculated from the frequency of bubble formation and the average volume of gas bubbles, determined from image analysis of the mean lengths of liquid and gas plugs, L_{liq} and L_{gas} , respectively, under a given set of flow conditions. This method of flow calculation has been previously employed in the context of gas–liquid multiphase flow in the microfluidic device.^{42,49,50} Actual flow parameters pertaining to the gas–liquid segmented microfluidic reactor experiments are described in Table S1, Supporting Information. For all experiments, the relative gas-to-liquid flow ratio ($Q_{\text{gas}}/Q_{\text{liq}}$) was ~ 1 , and two different nominal total flow rates were investigated: $Q = \sim 5$ $\mu\text{L}/\text{min}$ (low flow rate case) and ~ 50 $\mu\text{L}/\text{min}$ (high flow rate case) (see Table S1 for actual values).

On-Chip Micelle Preparation. For microfluidic self-assembly experiments, three separate liquid streams were combined at equal flow rate to form gas-separated liquid plugs within the reactor: (1) a 1.0 wt % solution of PS(665)-*b*-PAA(68) single chains in 75/25 w/w DMF/dioxane; (2) a separator stream containing 75/25 w/w DMF/dioxane only; (3) a solution of 75/25 w/w DMF/dioxane containing 12.6, 15.6, or 21.6 wt % deionized water. Combination of the three liquid streams yielded steady-state on-chip concentrations of 0.33 wt % polymer, identical to the off-chip control experiments, and either 4.2, 5.2, or

7.2 wt % water, 1.0, 2.0, and 4.0 wt % above the *cwc* (3.2 wt %), respectively. Microfluidic flow conditions were selected as described in the previous section.

For off-chip analysis of micelle morphologies prepared within the reactor, micellar dispersions were generally collected from the chip following the processing channel into vials containing a large excess ($\sim 250 \mu\text{L}$) of deionized water, where the particles immediately became kinetically frozen due to the high water content. For experiments tracking the off-chip relaxation of micellar morphologies formed on-chip, micellar dispersions were collected from the chip following the processing channel into empty vials; the solutions were then allowed to sit off-chip without shear or stirring for various times, before kinetic trapping by dumping into excess deionized water. For both types of micelle collection (immediate trapping or annealing), the solids content of the final mostly aqueous solution was $\sim 0.25 \text{ mg/mL}$.

Flow visualization of microfluidic experiments and quantification of all the flow conditions was performed with an inverted fluorescence microscopy system operating in transmission mode. Optical images of the reactor were captured using a CCD camera (AF6000 Orca, Hamamatsu, NJ) installed on the inverted microscope (DMI 6000B, Leica, Allendale, NJ).

TEM and Image Analysis. Transmission electron microscopy (TEM) of various aqueous micellar dispersions was performed on a Hitachi H-700 electron microscope, operating at an accelerating voltage of 75 kV. For TEM imaging, a $10 \mu\text{L}$ drop of micellar dispersion was deposited onto either a carbon-coated or carbon-coated Formvar 300 mesh copper grid and then shadowed with Pt/Pd wire for imaging. For TEM imaging of on-chip prepared samples, the small quantity of dioxane remaining in the final solutions was found to dissolve Formvar substrates, and so carbon-coated grids without Formvar were required for these samples.

Analysis of micelle size distributions and statistics of both spherical and nonspherical aggregates were carried on images randomly selected from various regions of the TEM grid. To assemble size histograms of spherical micelle populations for each sample, the diameters of 150 spheres were measured with a caliper (Mastercraft, Boynton Beach, FL), from printouts of multiple regions of the TEM grid where the particles appeared 40 000 to 50 000 times their actual size.

To quantify the percentage of nonspherical micelles in a given sample, we determined their areal percentage relative to the total micelle area in TEM images. Assuming a constant density and constant height of different micelle morphologies on the TEM grids, the areal percentage of nonspherical micelles gives a reasonable estimate of their weight percentage relative to total micelles in a given sample. The areal percentage of nonspherical micelles on a TEM grid was averaged from values determined from four to five randomly selected regions. When a grid region was selected, a low-magnification (10k) image was first taken, followed by higher-magnification (20k) imaging of four quadrants of the larger area to allow for accurate image analysis. The higher magnification images were processed with scientific image analysis software (ImageProPlus v. 6.1, Media Cybernetics). Appropriate brightness, contrast, and sharpness levels were selected for each image; after image binarization, threshold levels were set to allow particles to be counted and analyzed by the software. By visual inspection, nonspherical objects were then selected and their areal percentage was calculated. For each sample, the process was repeated for two other TEM grids prepared using the same micelle dispersion, in order to arrive at an average value and experimental error (standard deviation of the three grids) for the sample. The experimental errors on values of the areal percentage of nonspherical micelles in various samples were $\sim 15\text{--}20\%$.

It was found that dynamic light scattering (DLS) analysis of many of the micelle populations prepared on-chip was not practical for two reasons. First, the samples could not be effectively filtered to remove dust without also removing many of the larger nonspherical micelles in

the sample. Second, the small number of fractions and very slow diffusion times for the large network micelles observed in many on-chip prepared samples did not allow them to be effectively sampled in typical collections of the DLS autocorrelation function.

Zeta Potential Measurements. Zeta potentials of various samples were measured using a Zeta PALS Analyzer (Brookhaven Instruments Corporation, Holtsville, NY). Zeta potential values were computed from electrophoretic mobility values at $25 \text{ }^\circ\text{C}$ using the Smoluchowski equation.

RESULTS AND DISCUSSION

The specific amphiphilic block copolymer used for this study is polystyrene-*block*-poly(acrylic acid), PS(665)-*b*-PAA(68), where numbers in brackets indicate number average degrees of polymerization for the respective blocks. For all on-chip and off-chip (control) experiments, solutions of 0.33 wt % PS(665)-*b*-PAA(68) in the solvent mixture 75/25 (w/w) *N,N*-dimethylformamide/1,4-dioxane (DMF/dioxane) serve as the initial state for block copolymer self-assembly. Subsequent water addition to the solution in the microfluidic device (on-chip) or in vials (off-chip) increases the polarity of the solvent and decreases the solubility of the hydrophobic PS blocks until micelles with PS cores and soluble PAA coronae are formed (Figure 1A). In both bulk and microfluidic environments, micelle formation is thermodynamically favorable above the critical water concentration (*cwc*),⁷ which is determined to be $3.2 \pm 0.1 \text{ wt } \%$ for the copolymer solution employed here (Figure S1). Therefore, to investigate the effect of the chemical environment on self-assembly, three different water contents, 1, 2, and 4 wt % *above the cwc*, were selected for on-chip and off-chip experiments: that is, 4.2, 5.2, and 7.2 wt % water in DMF/dioxane.

Microfluidic self-assembly in the gas-liquid segmented reactor is depicted in Figure 1B. A stream of the DMF/dioxane solvent mixture containing PS(665)-*b*-PAA(68) copolymer is combined with a DMF/dioxane separator stream and a DMF/dioxane/water stream; the concentrations of copolymer and water in the corresponding inlet streams are selected to give a cross-sectional average copolymer concentration of 0.33 wt % and a cross-sectional average water concentration of 4.2, 5.2, or 7.2 wt %. The streams are then joined with argon gas at the injector, which compartmentalizes the colaminar flow into liquid plugs. The resulting chaotic advection in the sinusoidal mixing channel enables fast mixing of water with the copolymer solution ($\sim 1 \text{ s}$),^{41,42,51,52} triggering micelle formation shortly after the injector.

A detailed schematic of the reactor is shown in Figure 1C. The reactor has a set channel depth of $150 \mu\text{m}$ and consists of a sinusoidal mixing channel $100 \mu\text{m}$ wide and 100 mm in length, and a sinusoidal processing channel $200 \mu\text{m}$ wide and 740 mm in length. Following initial formation, block copolymer micelles are exposed to continuous mixing as the liquid plugs proceed through the mixing and processing channels, until the colloidal dispersion is collected at the outlet for off-chip characterization by transmission electron microscopy (TEM). Unless otherwise stated, micelles formed on-chip are kinetically trapped immediately upon exiting the chip by collection into a vial containing a large excess of deionized water; under these conditions, the amount of organic solvent in the PS phase becomes negligibly small, and micelle cores that were highly dynamic on-chip as a result of solvent swelling become suddenly vitrified, “freezing” the on-chip colloidal morphologies for off-chip characterization.

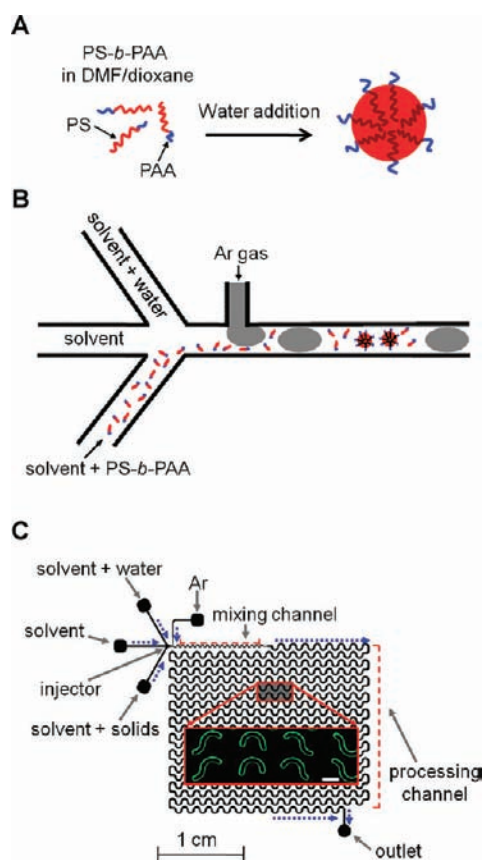


Figure 1. PS-*b*-PAA self-assembly process and multiphase microfluidic reactor approach. (A) Schematic of the PS-*b*-PAA assembly process. Red indicates hydrophobic PS blocks, while blue indicates hydrophilic PAA blocks. (B) Cartoon representation of the self-assembly of PS-*b*-PAA into micelles in the multiphase microfluidic reactor. The self-assembly is initiated by mixing of the three liquid stream contents within segmented plugs, which leads to an average cross-streamwater content above the critical water content (cwc). (C) Schematic of the microfluidic reactor, showing liquid and gas inlets at the injector, followed by the mixing channel (represented in B); in the subsequent processing channel, the formed micelles experience the shear-induced collisions and morphological transformations discussed in the text, which are trapped by collection into pure water after the outlet. The inset of C shows a select optical microscopy image of the reactor under stable operation. The white scale bar indicates 500 μm.

For all experiments, the gas-to-liquid flow ratio is ~ 1 , and two different nominal total flow rates are investigated: $Q = \sim 5 \mu\text{L}/\text{min}$ (low flow rate case) and $\sim 50 \mu\text{L}/\text{min}$ (high flow rate case).⁵³ An optical image of part of the reactor (Figure 1C, inset) demonstrates typical stable operation in which uniform and regularly spaced gas bubbles are produced.

The dramatic effect of the microfluidic environment on micelle morphologies produced by block copolymer self-assembly is shown in Figure 2. In the off-chip control experiment, water is added dropwise to a solution of PS(665)-*b*-PAA(68) up to 5.2 wt %, and the resulting dispersion is allowed to equilibrate for 2 weeks, generating exclusively spherical micelles (Figure 2A, mean diameter, $d = 35 \text{ nm}$). In contrast, block copolymer self-assembly at the same water content in the microfluidic device operating at low flow rate ($Q = \sim 5 \mu\text{L}/\text{min}$) gives a mixture of spherical micelles ($d = 41 \text{ nm}$) and several higher order, nonspherical morphologies (Figure 2B–D). The representative

images highlight the broad range of morphologies that are generated on-chip under these conditions, including linear and looped cylinders, Y-junctions, spherical caps, bilayer sheets, and dense networks of loops and cylinders. Several of the larger micelles consist of hybrid morphologies described by abrupt changes in local interfacial curvature. For example, the micellar aggregate in Figure 2C possesses interconnected bilayer regions with appendages of linear and looped cylinders, while Figure 2D shows a flat bilayer sheet embedded within a network of looped cylinders and Y-junctions.

On the basis of their uniformity and low polydispersity, we expect that the spherical micelles formed off-chip (Figure 2A) are close to thermodynamic equilibrium. Conversely, the various nonspherical morphologies (Figure 2B–D) formed under identical chemical conditions but in the microfluidic device appear to be kinetic products of the unique on-chip environment. Our previous work on similar two-phase microfluidic reactors has shown that recirculating flow in the liquid plugs gives rise to localized regions of extremely high shear ($\sim 10^4$ to 10^5 s^{-1}) in the plug corners.⁴¹ Moreover, we have demonstrated that the associated shear fields can induce both coalescence and breakup of suspended, solvent-swollen polymeric particles, with shear-induced coalescence dominating at low flow rate ($\sim 5 \mu\text{L}/\text{min}$) and shear-induced breakup becoming increasingly important at higher flow rates.⁴² In the current work, we attribute the various nonspherical micelle morphologies formed at $5 \mu\text{L}/\text{min}$ (Figure 2) to shear-induced coalescence of smaller, more thermodynamically stable, spherical micelles within the microfluidic reactor.

The free energy pathway for such on-chip shear-induced morphology transitions is represented in Scheme 1. First, spherical micelles are generated shortly after the injector, as fast mixing of water ($< 1 \text{ s}$) brings the average solvent composition above the cwc (Scheme 1, State A). Next, as the liquid plugs travel through the reactor, continuous recirculating flow moves micelles in and out of the high-shear corners, resulting in shear-induced micelle coalescence to form larger micelles with elevated free energies compared to the global equilibrium state (Scheme 1, State B). Finally, internal chain rearrangements, driven by localized free energy lowering within coalesced micelles, give rise to the various nonspherical morphologies (Scheme 1, State C).

Shear-induced aggregation of solid colloidal particles (or coalescence of liquid drops) is a well-known phenomenon occurring in both natural and industrial systems, with examples ranging from the deterioration of dispersed pigments to the formation of strong silk fibers within a spider's spinneret.⁵⁴ Recent theoretical work by Zaccone and co-workers describes shear-induced aggregation as an activated-rate process, using an Arrhenius-type rate equation to show that shear both increases the particle collision rate and also supplies energy to overcome repulsive interparticle potentials, thus increasing the fraction of adhesive collisions.⁵⁵ In general, the relative effects of shear and Brownian motion on aggregation rates of colloidal particles can be described by the dimensionless Peclet number:

$$Pe = \frac{\dot{\gamma} a^2}{D_0} \quad (1)$$

where $\dot{\gamma}$ is the shear rate, a is the particle size and D_0 is the particle diffusion coefficient.⁵⁶ For low Peclet numbers ($Pe \ll 1$), thermal diffusion has a dominant effect on particle aggregation, whereas

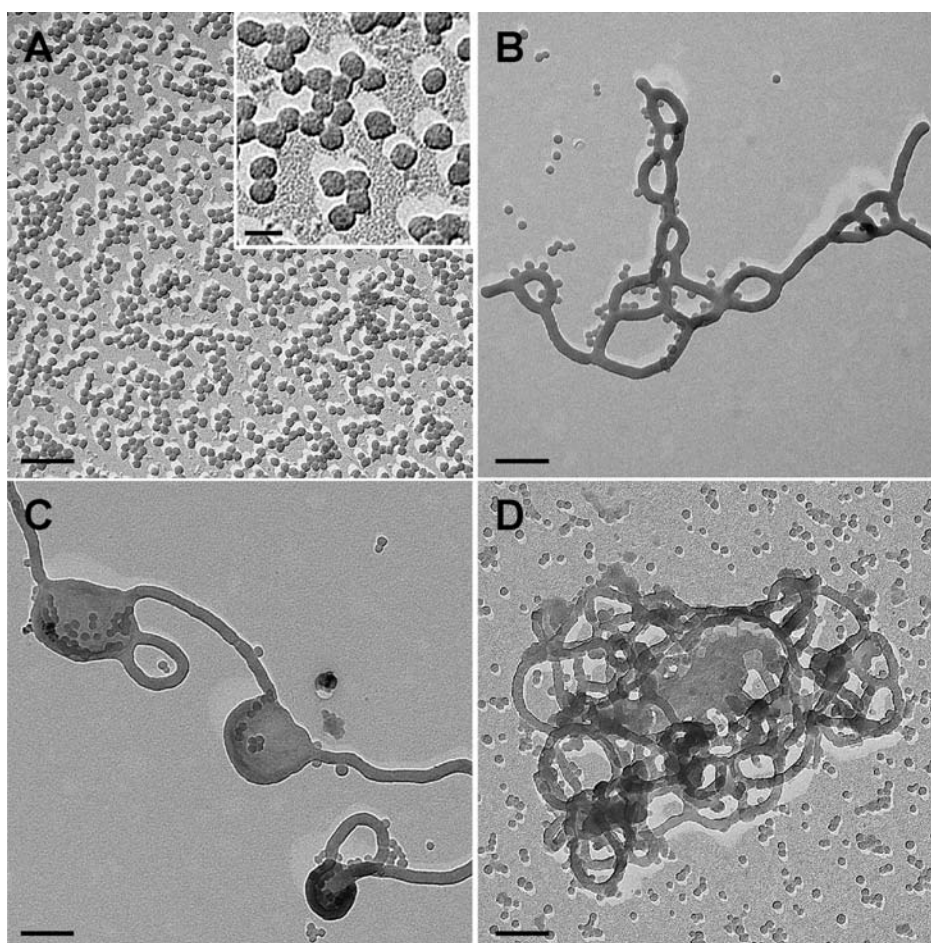


Figure 2. TEM images comparing off-chip (A) and on-chip, $Q = \sim 5 \mu\text{L}/\text{min}$ (B–D), morphologies of PS-*b*-PAA micelles formed in DMF/dioxane mixtures containing 5.2 wt % water. Only the equilibrium spherical morphology was formed off-chip (A). However, the on-chip experiment yielded a mixture of morphologies in addition to spheres, including linear and looped cylinders (B, C, and D), Y-junctions (B and D), spherical caps (B), bilayer sheets (C and D), and networks (D). All scale bars = 200 nm, except the higher-magnification inset to A (scale bar = 50 nm).

shear forces have a stronger influence on aggregation rates as Peclet numbers increase.⁵⁷

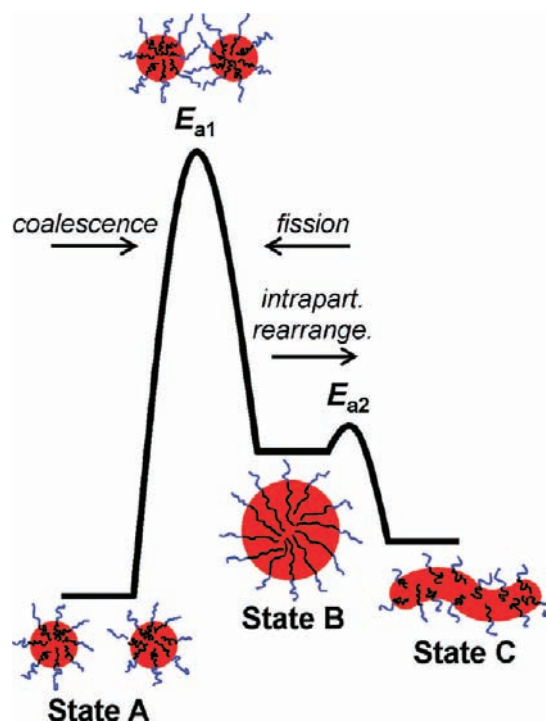
From eq 1, the initially formed spherical micelles ($a = \sim 40 \text{ nm}$) in the high-shear corners of the liquid plugs at low flow rate ($\dot{\gamma} = \sim 10^4 \text{ s}^{-1}$) are described by a Peclet number of $Pe = \sim 10$.⁵⁸ Although the specific dependence of shear-induced aggregation on Pe depends on the nature of the interparticle interactions,⁵⁶ Pe numbers on the order of ~ 10 have been found to give rise to shear-induced aggregation in related systems.^{55–57} It is therefore reasonable to propose that micelles will experience multiple shear-induced collisions as they circulate through the high-shear hot spots of the plug corners, with some of these collisions being sufficiently energetic to overcome E_{a1} (Scheme 1) and activate micelle coalescence.⁵⁵ The collision of two primary micelles, represented in Scheme 1, is only one of many statistical possibilities, which will also include collisions between one or more larger micelles (with higher Peclet numbers, eq 1) that have experienced at least one previous instance of collision–coalescence.

A key component of the activation energy E_{a1} is the repulsion between the overlapping coronae of colliding micelles (Scheme 1).⁵⁹ Even at the relatively low water contents in DMF/dioxane employed on-chip (~ 4 – $7 \text{ wt } \%$), PS-*b*-PAA micelles will exhibit polyelectrolyte character, due to preferential accumulation of

water within the PAA corona.⁶⁰ This means that the PAA chains will be partially ionized and negatively charged, with the extent of ionization increasing at higher water contents; this was confirmed by off-chip zeta-potential measurements of PAA-*b*-PAA micelles at the same solvent conditions as on-chip experiments, which gave $\zeta = -22 \pm 4$, -30 ± 2 , and $-33 \pm 2 \text{ mV}$ in DMF/dioxane at 4.2, 5.2, and 7.2 wt % water, respectively.

To estimate the contribution of intercoronal repulsion to E_{a1} , we employ a recent model by Jusufi et al. describing repulsive interactions between spherical polyelectrolyte brushes.⁵⁹ According to this model, the confinement of counterions within the brush layers results in negligible electrostatic interparticle forces. As well, it is assumed that chains in the approaching brushes retract from each other (or “dent”) rather than interdigitating. The dominant term of the resulting electrosteric pair potential is attributed to the decreased entropy of counterions in the overlapping polyelectrolyte brushes. The analytical form of their result is a pair potential that increases from zero as approaching brushes begin to overlap and reaches a maximum value of $0.2kT$ per unit counterion when the cores come into contact. From this result, we take $0.2kT \times (Q/|e|)$ as the electrosteric contribution to E_{a1} , where Q is the effective charge of counterions in the corona and e is the elementary charge.

Scheme 1. Proposed Energy Diagram for On-Chip Shear-Induced Morphological Transitions



For spherical micelle cores with $a \sim 40$ nm, an aggregation number of $Z \sim 250$ is determined, or $\sim 2 \times 10^4$ COOH units per micelle. Assuming a maximum degree of ionization of $\sim 10\%$ (calculated from a pK_a of 4.25 in water),⁶⁰ and two-thirds condensed counterions,⁵⁹ we obtain an effective charge of counterions in the corona of $Q \sim 700 |e|$, which yields an E_{a1} value on the order of $\sim 100kT$ if electrosteric effects dominate the coalescence energy barrier.

Another potential contribution to E_{a1} is the viscosity of the PS micelle cores, which will govern the rate of core coalescence if the electrosteric barrier described above is overcome. It is well established that block copolymer intermicellar and intramicellar chain dynamics are a strong function of the water content in polar organic solvents; at low water contents, the micelle cores are highly swollen by the organic solvent, becoming increasingly viscous until eventual kinetic freezing as the water content increases.^{8,10} For PS-*b*-PAA in DMF, fast micelle equilibration kinetics on experimental time scales for water contents less than $\sim 6.5\%$ have been found, suggesting highly swollen and dynamic PS blocks in this range of solvent composition;¹⁰ based on this result, and considering that dioxane is an even better solvent for the PS core than DMF,⁸ it is reasonable to conclude that core viscosities do not contribute significantly to E_{a1} in DMF/water mixtures at the two lowest water contents of 4.2 and 5.2 wt %. However, as the water content increases, the solvent content in the core, along with the chain dynamics, will drop off significantly; we therefore cannot rule out a considerable, and possibly even dominant, contribution of core viscosity to the coalescence rate at the highest water content (7.2 wt %).

From the Arrhenius expression for the rate of shear-activated coalescence,⁵⁵ a critical shear rate $\dot{\gamma}^*$ can be defined such that the activation barrier becomes vanishingly small, and the rate of

coalescence becomes equal to the collision rate, when $\dot{\gamma} \gg \dot{\gamma}^*$:

$$\dot{\gamma}^* = \frac{E_{a1}}{6\pi\alpha\mu a^3} \quad (2)$$

In this expression, α is a numerical coefficient describing the flow (e.g., $\alpha = 1/3\pi$ for simple shear) and μ is the dynamic viscosity. Using $E_{a1} = 100kT$, $\alpha = 1/3\pi$, $\mu = 0.001$ Pa s, and $a = 40$ nm, we obtain $\dot{\gamma}^* = 6 \times 10^6$ s⁻¹ for primary spherical PS-*b*-PAA micelles in DMF/water with electrosteric repulsion. Because in the high-shear hot spots on chip $\dot{\gamma}^* \gg \dot{\gamma} \sim 10^4$ s⁻¹, we conclude that the magnitude of E_{a1} will strongly influence the kinetics, such that the rate of shear-induced coalescence is expected to increase as E_{a1} decreases with decreases in coronal charge or core viscosity.⁵⁵

As the average micelle size increases through statistical collision-coalescence events, increased PS chain stretching stores accumulated shear energy in micelles with elevated free energies (Scheme 1, State B). Outside of the high-shear regions, coalesced micelles in State B will therefore have a thermodynamic tendency to return to their lowest free energy state via micelle fission (Scheme 1). However, if a sufficiently high E_{a1} results in a fission rate that is comparable or slow compared to the rate of shear-induced coalescence, then on-chip relaxation to global equilibrium will be precluded. Under this kinetic constraint, a significant number of micelles in State B will lower their free energy via the alternative pathway of intramicellar chain rearrangements, leading to localized morphology transitions (State C). The energy barrier E_{a2} is expected to be a function of the viscous resistance to intramicellar chain diffusion within the PS cores; at low water contents (4–5 wt %), the PS cores will be highly swollen with solvent, with estimated core polymer concentrations of ~ 50 wt %.⁸ Using literature values for the activation energy of viscous flow for PS-toluene solutions of similar concentrations,⁶¹ we estimate E_{a2} to be $\sim 10kT$, 1 order of magnitude lower than E_{a1} . This explains why the intramicellar pathway to the observed nonspherical morphologies is kinetically favored over a return to global equilibrium. Therefore, as a combined result of the statistical nature of shear-induced collisions and the kinetic constraints of relaxation processes in the microfluidic device, we obtain a potpourri of spherical and nonspherical morphologies that are not globally equilibrated but nonetheless represent a tendency of micelles to locally minimize their internal free energy.

Although the details of these on-chip morphological transformations are currently unknown, copolymer chains within a coalesced micelle are assumed to redistribute following microphase separation principles, with internal curvature optimized to reduce chain stretching within the constraints of high packing densities required to lower the interfacial tension.^{1,2,13,34} In general, micelle morphologies will change from spheres to cylinders to bilayer structures (in order of decreasing internal curvature), as a means of relieving stretching of core-forming blocks in response to chemical variables that increase the chain packing density at the interface.^{1,2} In the present case, it is shear-induced coalescence, rather than chemical forces, that locally increase aggregation numbers, triggering localized transitions from spheres to mainly cylindrical structures in order to lower internal curvature and reduce PS stretching. However, despite the predominance of cylinders under the current chemical and flow conditions, we point out that other nonspherical morphologies with even lower internal curvature are also observed, suggesting significant variability in local conditions due to the

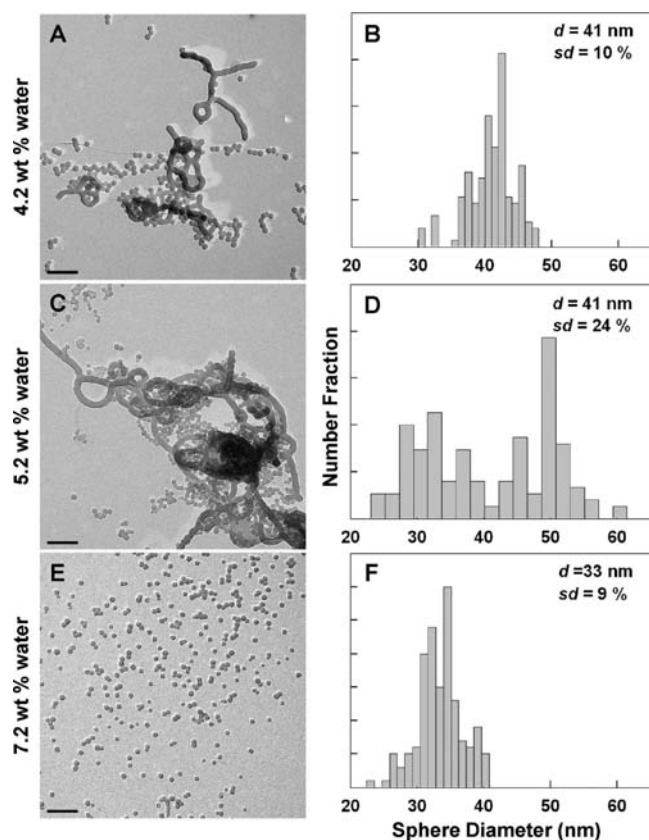


Figure 3. The effect of water content on on-chip PS-*b*-PAA micelle morphologies (A, C, and E) and spherical micelle size distributions (B, D, and F) formed in DMF/dioxane mixtures, $Q = \sim 5 \mu\text{L}/\text{min}$. A, C, and D show TEM images of representative micelles formed at 4.2, 5.2, and 7.2 wt % water, respectively; B, D, and F show size histograms of spherical micelle populations formed at the corresponding water contents. All scale bars = 200 nm.

statistical nature of collision-coalescence events. For instance, the observed hybrid morphologies discussed earlier (e.g., Figure 2, C and D) are explained by intraparticle morphology transitions (e.g., from cylinders to bilayers) that become kinetically trapped during off-chip collection.

Recently, Winnik and co-workers showed that a sphere-to-wormlike network transition could be induced in polystyrene-*block*-poly(4-vinylpyridine) (PS-*b*-P4VP) block copolymer micelles with PS cores and P4VP coronae by conventional rapid magnetic stirring at 1200 rpm but only in the presence of CdSe quantum dots, which were proposed to form bridging interactions between coronae of assembling spherical micelles.²⁹ Therefore, to confirm the important role of the extremely strong shear fields enabled by the on-chip environment in the current system,⁴¹ we investigate the effect of micelle formation under off-chip vigorous magnetic stirring conditions similar to those employed in ref 34. In this experiment, micelles are formed by dropwise addition of water to 5.2 wt % and then stirred at 1200 rpm for 280 s (equivalent to the on-chip residence time at low flow rate). Although the solution mixing will be much improved, the maximum shear rates in this experiment are on the order of 1 s^{-1} , which are negligible compared to local maxima experienced on-chip. In contrast to on-chip self-assembly under the same chemical conditions, no nonspherical micellar structures are formed in these more conventional shear fields, and the

Table 1. Mean Spherical Micelle Diameters under Various On-Chip and Off-Chip Preparation Conditions

conditions	4.2 wt % water	5.2 wt % water	7.2 wt % water
	Off-Chip		
	29 nm	35 nm	39 nm
	On-Chip, $\sim 5 \mu\text{L}/\text{min}$		
$t = 0$	41 nm ^a	41 nm ^a	33 nm
$t = 2 \text{ h}$	41 nm ^a	36 nm ^a	—
$t = 10 \text{ h}$	45 nm ^a	36 nm ^a	—
$t = 48 \text{ h}$	49 nm ^a	35 nm ^a	—
$t = 7 \text{ days}$	49 nm	35 nm ^a	—
$t = 28 \text{ days}$	49 nm	35 nm	—
	On-Chip, $\sim 50 \mu\text{L}/\text{min}$		
	37 nm	32 nm	30 nm

^a Indicates sample containing nonspherical micelles, in addition to the spherical micelles measured here.

resulting spherical micelles are similar in size ($d = 37 \text{ nm}$) to micelles formed off-chip at 5.2 wt % water without vigorous stirring ($d = 35 \text{ nm}$, Figure S2). We conclude that nanoscale velocity gradients in the plug corners are germane to increasing the rate of on-chip collision-coalescence events relative to normal diffusive motion in the bulk, thus enabling the morphology transformations described above.

Figure 3 describes the effect of chemical conditions on the on-chip formation of flow-directed block copolymer micelle morphologies at low flow rate. In Figure 3A,C,D, representative micelles are shown for solvent mixtures with 4.2, 5.2, and 7.2 wt % water, with associated spherical micelle size distributions shown in Figure 3B,D,F. Not shown in the figure are the results of the associated off-chip control experiments, which give rise to uniform and low-polydispersity spherical micelles for all three water contents, with monotonically increasing mean sphere sizes of 29 nm, 35 nm, and 39 nm for 4.2, 5.2, and 7.2 wt % water, respectively (Table 1). Comparing 4.2 and 5.2 wt % water on-chip (Figure 3A,C), both images reveal a mixture of spheres and nonspherical morphologies, indicating that shear-induced morphological transformations are operative at both water contents. In addition, both samples show spherical micelle populations with the same mean size ($d = 41 \text{ nm}$), larger than the associated off-chip equilibrium sizes ($d = 29$ and 35 nm for 4.2 and 5.2 wt % water, respectively), although with very different distribution shapes and widths (Figure 3B,D). We also find that the higher water content results in significantly larger network structures (Figure S3), as well as a higher areal percentage of nonspherical micelles relative to the total micelle area (areal percentage = 5% and 24% at 4.2 and 5.2 wt % water, respectively).⁶² This indicates that a significantly larger percentage of spherical micelles are converted into nonspherical nanostructures by the on-chip environment at 5.2 wt % compared to 4.2 wt % water. Interestingly, the opposite trend is found upon further increasing the water content to 7.2 wt % (Figure 3E), which results in uniform spherical micelles with mean size $d = 33 \text{ nm}$ (Figure 3F), smaller than the associated equilibrium value ($d = 39 \text{ nm}$), with no observable nonspherical micelles.

The influence of water content on the on-chip morphologies can be understood in terms of its effect on activation barriers in Scheme 1. The activation energy for the coalescence/fission

process, E_{a1} , is a function of intercoronal electrosteric repulsion and core viscosity for two colliding micelles, which represents the transition state between States A and B.⁶³ With increasing water content, intercoronal repulsion and core viscosity will both increase, as the PAA chains become increasingly ionized and the solvent quality for the PS core decreases.¹⁰ Both effects will therefore contribute to an increase in E_{a1} , and the latter effect will also contribute to an increase in E_{a2} . The increase in electrosteric interactions will dominate at the two lowest water contents (4.2 and 5.2 wt %), where the electrosteric barrier for coalescence is $\sim 10\times$ greater than the barrier for viscous flow within the core. However, the increase in core viscosity is expected to play a more significant role at 7.2 wt % water, based on the demonstrated sharp decrease in PS-*b*-PAA chain dynamics for water contents >6.5 wt %.¹⁰

For an intermediate value of E_{a1} , sufficiently low for shear-induced coalescence to be activated but sufficiently high to significantly inhibit the reverse fission process, a large number of high-energy micelles will be trapped on the right-hand-side of the coalescence/fission activation barrier. This situation is consistent with the bimodal nature of the spherical micelle distribution at 5.2 wt % (Figure 3D), in which two distinct populations of smaller and larger particles correspond to micelles in States A and B, respectively. In contrast, when E_{a1} is lowered by decreasing the water content (e.g., to 4.2 wt % water), a faster fission rate leads to a more dynamic exchange between States A and B, resulting in a single averaged population of spherical micelles (Figure 3B). As well, the larger barrier E_{a1} at 5.2 wt % compared to 4.2 wt % forces a greater number of micelles in State B to follow the relatively fast intraparticle relaxation pathway through E_{a2} , explaining the larger quantity of nonspherical micelles in the former case. Conversely, when the water content is increased to the point where E_{a1} is too high for micelle coalescence to be activated (e.g., to 7.2 wt % water), the formation of nonspherical morphologies is precluded, and only spherical micelles are observed (Figure 3E).

The effect of flow rate on microfluidic block copolymer self-assembly was also determined, by investigating micelles prepared at the same three water contents but at high flow rate (~ 50 $\mu\text{L}/\text{min}$, Figure S4, Supporting Information). In contrast to the low flow rate case, only unimodal populations of spherical micelles, with no additional morphologies, are observed for all three water contents. According to our previous results on kinetic polymeric particles formed in similar reactors, the on-chip competition between shear-induced particle coalescence and shear-induced particle breakup favors coalescence at low flow rates and breakup as the flow rate increases.⁴² Therefore, for the 4.2 and 5.2 wt % water contents, when the flow rates are increased to ~ 50 $\mu\text{L}/\text{min}$, the shear-induced coalescence that gives rise to nonspherical morphologies at ~ 5 $\mu\text{L}/\text{min}$ (Figure 3, parts A and C, respectively) is countered by the dominant mechanism of shear-induced particle breakup, such that cylinders and other higher-aggregation structures cannot form.

On the basis of the current results, we believe that two alternative mechanisms for the on-chip morphology transformations can be ruled out. The first of these is a shear-induced micellization picture, described in the theoretical work of Jones et al.,⁶⁴ in which micellized states are influenced by shear forces at the stage of unimer self-assembly. To eliminate this possible mechanism, we consider that only a very small percentage of micelles will initially form under significant shear, due to the strong localization of high-shear regions in the plug corners. Specifically, a conservative calculation shows that less than 2% of

the liquid plug volume is exposed to the high shear regions during the initial mixing/micellization process.⁶⁵ The large percentages of nonspherical structures that we observe under certain conditions (up to 25% of the total micelle volume) cannot, therefore, be accounted for by micellization under shear. While it is not possible to completely shelter the bulk liquid from high shear during the short mixing process, the rapid mixing achieved with the multiphase microfluidic system effectively separates the mixing function, which initiates micelle formation, from the downstream shear processing function, which induces the morphological transformation.

A second mechanism that merits consideration is one in which the directionality of shear forces templates the formation of specific micelle morphologies. For example, cylindrical micelles could be formed via the one-dimensional assembly of spherical micelles along the direction of shear. However, we eliminate such a “shear-templating” mechanism based on the presence of other, nondirectional, morphologies such as bilayer sheets (Figure 2, C and D) which also form as a result of shear exposure. Rather, as described above, our results strongly support a mechanism in which the role of on-chip shear forces is simply to increase the rate of micelle coalescence in a statistical manner, such that colloids with aggregation numbers well above the mean equilibrium value are generated. The subsequent relaxation of these aggregates via intramicellar pathways is then guided by internal molecular forces (and not shear forces), ultimately forming the micelle morphology that allows the greatest decrease in local free energy relative to the initial shear-induced aggregation state.

Several of the on-chip morphologies formed at low flow rate, including looped cylinders, Y-junctions, and networks of linear and looped cylinders, are very reminiscent of nonergodic micelles of poly(1,2-butadiene)-*block*-poly(ethylene oxide) (PB-*b*-PEO) in aqueous solution described previously by Bates and co-workers.¹³ Although micelles in that work were not formed in the presence of strong external shear fields, the morphological similarities with our system are consistent with on-chip micelles being nonergodic on the time scale of our microfluidic experiments. In the work of Bates, complex micelles with unusual mirror symmetry were attributed to network fragmentation by stirring or sonication followed by intraparticle redistribution of molecules to balance the free energy, under conditions where interparticle exchange of material could not occur on experimental time scales.¹³ Interestingly, in addition to cylinder network fragments of various sizes formed on-chip (e.g., Figure 4A), we find a number of compelling complex micelles with mirror symmetry (Figure 4B–E). This further highlights the importance of intraparticle chain rearrangements in the on-chip formation of the observed micelle morphologies.

In contrast to PB-*b*-PEO micelles in water, which showed nonergodic behavior over a time scale of months to years, the off-chip relaxation of PS-*b*-PAA micelles formed on-chip can be monitored over a time scale of days to weeks (Figure 5). For relaxation studies, micellar dispersions are collected from the chip and allowed to sit for various times (t) before kinetic trapping by dumping into excess water; $t = 0$ represents samples collected with immediate off-chip trapping, giving a mixture of spherical and nonspherical morphologies as discussed above (Figure 5, A and C, for 4.2 and 5.2 wt % water, respectively). As shown in Figure 5, B and D, after sufficient off-chip time for both water contents, $t = 7$ days for 4.2 wt % (Figure 5B) and $t = 28$ days for 5.2 wt % (Figure 5D), the nonspherical micelles

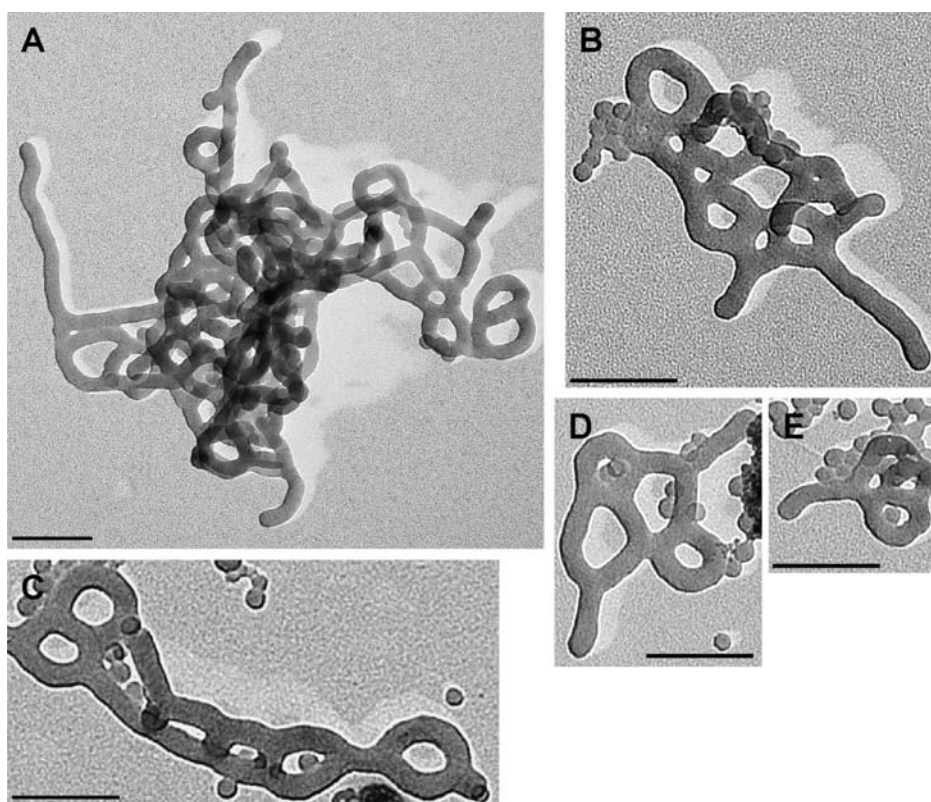


Figure 4. Further examples of PS-*b*-PAA micellar structures formed on-chip, $Q = \sim 5 \mu\text{L}/\text{min}$, in DMF/dioxane mixtures containing 4.2 wt % water (A, B, D, and E) or 5.2 wt % water (C). TEM images B–E highlight the prominent occurrence of nonspherical micelles with mirror image symmetry from on-chip self-assembly. All scale bars = 200 nm.

disappear completely, leaving only uniform populations of spheres. Because spherical micelles have been shown to be the equilibrium morphology at both of these water contents, the disappearance of nonspherical micelles is consistent with the relaxation of shear-induced structures toward global equilibrium, following their transfer to off-chip quiescent conditions. Note that the times required for the disappearance of cylindrical structures, on the time scale of days, are extremely long compared to the on-chip residence time (280 s); this explains why significant on-chip relaxation does not occur, such that shear-induced morphologies could be kinetically trapped off-chip for observation.

The off-chip relaxation kinetics of nonspherical micelles can be quantified by tracking the time-dependent decrease of their relative area for 4.2 and 5.2 wt % water dispersions. Because these samples show different initial percentages of nonspherical micelles, as discussed earlier, the two decay functions are compared by normalizing each data point with respect to the initial areal percentage value at $t = 0$. Figure 5E shows the resulting decay plots for 4.2 and 5.2 wt % water cases, indicating slower off-chip disappearance of nonspherical structures at higher water content. We found that neither data set could be fit to a single exponential decay, although both plots fit reasonably well to biexponential decay functions:

$$\text{rel area nonspherical micelles} = ae^{-t/\tau_1} + be^{-t/\tau_2} \quad (3)$$

The individual fast and slow decay times from the fit, τ_1 and τ_2 , are probably not physically meaningful, although they characterize the distribution of decay times in the collected samples.

Mean decay times for each fit were calculated using

$$\bar{\tau} = \left(\frac{a}{a+b} \right) \tau_1 + \left(\frac{b}{a+b} \right) \tau_2 \quad (4)$$

giving 26 s for the 4.2 wt % water sample and 5200 s (~ 2 h) for the 5.2 wt % water sample.

Along with different relaxation rates, a more detailed analysis of TEM images provides evidence for different off-chip relaxation mechanisms following on-chip micelle formation at 4.2 and 5.2 wt % water. The inset to Figure 5E shows an example of prominent aggregates observed between $t = 10$ min and $t = 120$ min in dispersions formed at 4.2 wt % water, which appear to be transition structures formed by cylinder networks breaking into spheres in the manner of Rayleigh instabilities in liquid strands.⁶⁶ The absence of similar structures during relaxation of the 5.2 wt % water sample suggests that cylinder breakup is not a prominent relaxation mechanism in that case, presumably due to stronger electrosteric repulsion between proximal spheres. This difference implies that the off-chip transition between nonspherical and spherical micelles at 5.2 wt % water occurs via the alternative relaxation mechanism of unimer exchange, with larger aggregates progressively releasing block copolymer chains into solution which then reassemble into more stable spheres.

Additional support for these different relaxation mechanisms comes from following the evolution of spherical micelle size distributions as a function off-chip time (Figure 6). Size distributions for 4.2 and 5.2 wt % water are shown on the left-hand and right-hand sides of the figure, respectively, for increasing off-chip times, t , moving down each column. The equilibrium (off-chip)

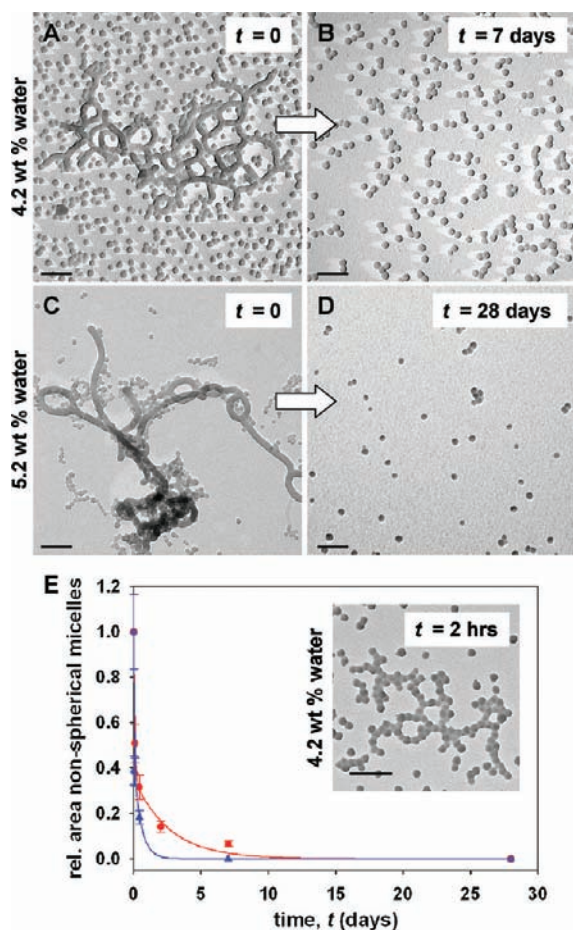


Figure 5. Off-chip relaxation kinetics of nonspherical micelles formed on-chip ($Q \sim 5 \mu\text{L}/\text{min}$) at two different water contents. A and C show TEM images of immediately trapped ($t = 0$) mixtures of spherical and nonspherical micelles formed at 4.2 and 5.2 wt % water, respectively. TEM images in B and D indicate that only spherical micelles remain at both water contents after sufficient off-chip relaxation time ($t = 7$ and 28 days for 4.2 and 5.2 wt % water, respectively). In E, the relative area of nonspherical micelles is plotted vs t for 4.2 wt % water (blue triangles) and 5.2 wt % water (red circles), with mean decay times of 26 and 5200 s, respectively, determined from fits to biexponential decay functions (solid blue and red curves). The inset to E shows an example of transition structures suggesting break-up of cylinders into spheres during off-chip relaxation at 4.2 wt % water. All scale bars = 200 nm.

mean sphere sizes for both water contents are indicated as a dashed line in the histograms. For 4.2 wt % water, no changes in the position and shape of the distribution are observed in the first 2 h off-chip ($d = 41$ nm), although by 10 h a clear shift to larger spherical micelles has occurred ($d = 45$ nm), away from the equilibrium sphere size ($d = 29$ nm). This unexpected shift can be explained by the process of cylinder breakup and the resulting generation of daughter spheres, whose sizes are governed by local wave instabilities that develop in the cylinder during relaxation rather than by a global free energy minimum. Following the near-complete disappearance of nonspherical micelles within ~ 1 day at 4.2 wt % water (Figure 5), the resulting spheres show no evidence of approaching their equilibrium size even after 28 days (Figure 6). We conclude that the relatively fast off-chip relaxation process of cylinder breakup leads to nonergodic spherical micelles kinetically trapped within a local free energy minimum.

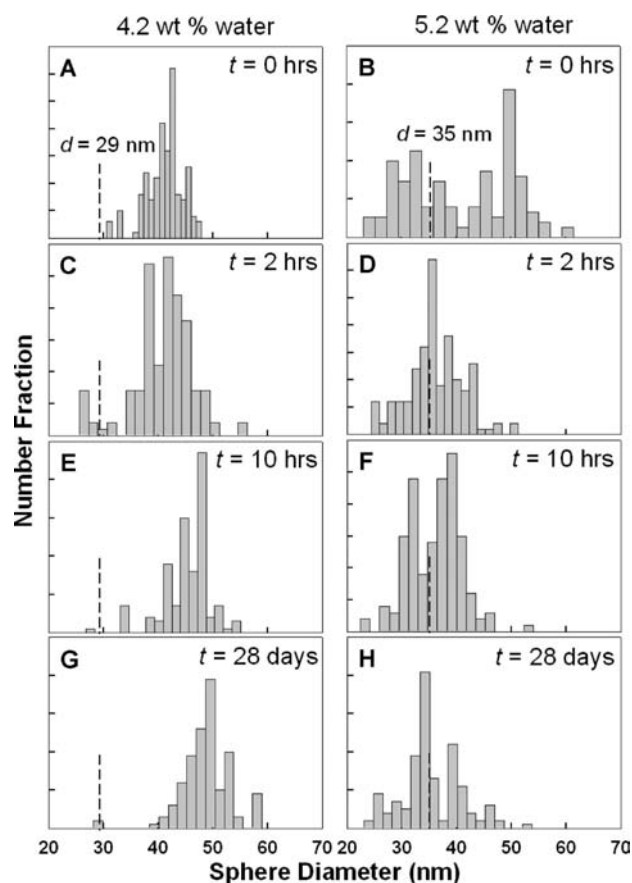


Figure 6. Evolution of spherical micelle size distributions as a function off-chip relaxation time, t , for the two on-chip samples (4.2 and 5.2 wt % water) described in Figure 5. The expected equilibrium mean size of spherical micelles under the same chemical conditions, based on off-chip micellization experiments at 4.2 or 5.2 wt % water followed by two weeks equilibration (Table 1), is indicated as a dashed line in the histograms.

In contrast, the size distributions of spherical micelles show very different off-chip evolution at 5.2 wt % water. In this case, the bimodal distribution discussed previously ($t = 0$) rapidly converges to a unimodal sphere population ($t = 2$ h, $d = 36$ nm) centered close to the equilibrium size ($d = 35$ nm), which then persists for the remainder of the monitored time off-chip. This trend corroborates the off-chip relaxation mechanism of unimer exchange at this water content. By this pathway, the cylinder networks disappear more gradually than by cylinder breakup (Figure 5), although in a manner that allows global equilibrium to be reached on a shorter time scale.

CONCLUSIONS

We have demonstrated that the solution self-assembly of amphiphilic block copolymers in a gas–liquid multiphase microfluidic reactor provides flow-directed variation of micelle morphologies due to the unique on-chip shear environment. Under chemical conditions that form equilibrium spherical micelles off-chip, a range of nonspherical nanostructures, including bilayer lamellae and networks of cylinders, can be generated on-chip. The resulting nanostructures are varied using a combination of chemical (bottom-up) and flow (top-down) parameters, and can be kinetically trapped off-chip by collection into excess water. A micelle formation mechanism of shear-induced collision–coalescence

followed by intraparticle chain rearrangements is proposed for microfluidic self-assembly. Finally, the off-chip micelle relaxation processes are analyzed under different chemical conditions. Top-down directed molecular self-assembly in microfluidic reactors opens up new opportunities for processing control of functional colloidal nanostructures for a wide range of applications ranging from imaging to drug delivery.

■ ASSOCIATED CONTENT

S Supporting Information. Data for critical water content determination; TEM images of micelles prepared off-chip with different stir rates; additional TEM images of nonspherical micelles generated on-chip at low flow rate and different water contents; TEM images and particle size distributions of spherical micelles generated on-chip at high flow and different water contents; actual measured flow data for various runs described in the text; relative standard deviations for data in Table 1. This information is available free of charge via the Internet at <http://pubs.acs.org/>.

■ AUTHOR INFORMATION

Corresponding Author

mmoffitt@uvic.ca

■ ACKNOWLEDGMENT

The authors are grateful for the financial support by the Natural Sciences and Engineering Research Council (NSERC) of Canada, through research grants to D.S., and MGM Infrastructure funding from the Canada Foundation for Innovation (CFI). British Columbia Knowledge Development Fund (BCKDF) is also gratefully acknowledged, along with a Collaborative Research Stipend from the Centre for Advanced Materials and Related Technologies (CAMTEC, UVic).

■ REFERENCES

- (1) Zhang, L.; Eisenberg, A. *Science* **1995**, *268*, 1728–1731.
- (2) Zhang, L.; Eisenberg, A. *J. Am. Chem. Soc.* **1996**, *118*, 3168–3181.
- (3) Yu, K.; Zhang, L.; Eisenberg, A. *Langmuir* **1996**, *12*, 5980–5984.
- (4) Zhang, L.; Yu, K.; Eisenberg, A. *Science* **1996**, *272*, 1777–1779.
- (5) Shen, H.; Zhang, L.; Eisenberg, A. *J. Phys. Chem. B* **1997**, *24*, 4697–4708.
- (6) Yu, Y.; Eisenberg, A. *J. Am. Chem. Soc.* **1997**, *119*, 8383–8384.
- (7) Zhang, L.; Shen, H.; Eisenberg, A. *Macromolecules* **1997**, *30*, 1001–1011.
- (8) Yu, Y.; Zhang, L.; Eisenberg, A. *Macromolecules* **1998**, *31*, 1144–1154.
- (9) Discher, B. M.; Won, Y.-Y.; Ege, D. S.; Lee, J. C.-M.; Bates, F. S.; Discher, D. E.; Hammer, D. A. *Science* **1999**, *284*, 1143–1146.
- (10) Zhang, L.; Eisenberg, A. *Macromolecules* **1999**, *32*, 2239–2249.
- (11) Shen, H.; Eisenberg, A. *J. Phys. Chem. B* **1999**, *103*, 9473–9487.
- (12) Discher, D. E.; Eisenberg, A. *Science* **2002**, *297*, 967–973.
- (13) Jain, S.; Bates, F. S. *Science* **2003**, *300*, 460–464.
- (14) Cui, H.; Chen, Z.; Zhong, S.; Wooley, K. L.; Pochan, D. J. *Science* **2007**, *317*, 647–650.
- (15) Wang, X. S.; Guerin, G.; Wang, H.; Wang, Y. S.; Manners, I.; Winnik, M. A. *Science* **2007**, *317*, 644–647.
- (16) Forster, S.; Plantenberg, T. *Angew. Chem., Int. Ed.* **2002**, *41*, 688–714.
- (17) Liu, G. *Adv. Polym. Sci.* **2008**, *220*, 29–64.
- (18) Li, Z.; Kesselman, E.; Talmon, Y.; Hillmyer, M. A.; Lodge, T. P. *Science* **2004**, *306*, 98–101.
- (19) Li, Z.; Hillmyer, M. A.; Lodge, T. P. *Nano Lett.* **2006**, *6*, 1245–1249.
- (20) Larue, I.; Adam, M.; Pitsikalis, M.; Hadjichristidis, N.; Rubinstein, M.; Sheiko, S. S. *Macromolecules* **2006**, *39*, 309–314.
- (21) Allen, C.; Maysinger, D.; Eisenberg, A. *Colloids Surf., B* **1999**, *16*, 3–27.
- (22) Geng, Y.; Dalhaimer, P.; Cai, S.; Tsai, R.; Tewari, M.; Minko, T.; Discher, D. E. *Nat. Nanotechnol.* **2007**, *2*, 249–255.
- (23) Gonzalez, D. C.; Savariar, E. N.; Thayumanavan, S. *J. Am. Chem. Soc.* **2009**, *131*, 7708–7716.
- (24) Torchilin, V. P. *Adv. Drug Delivery Rev.* **2002**, *54*, 235–252.
- (25) Nasongkla, N.; Bey, E.; Ren, J. M.; Ai, H.; Khemtong, C.; Guthi, J. S.; Chhin, S. F.; D., S. A.; Boothman, D. A.; Gao, J. M. *Nano Lett.* **2006**, *6*, 2427–2430.
- (26) Wu, W. C.; Chen, C. Y.; Tian, Y. Q.; Jang, S. H.; Hong, Y. N.; Liu, Y.; Hu, R. R.; Tang, B. Z.; Lee, Y. T.; Chen, C. T.; C., C. W.; Jen, A. K. Y. *Adv. Funct. Mater.* **2010**, *20*, 1413–1423.
- (27) Rockford, L.; Mochrie, S. G. J.; Russell, T. P. *Macromolecules* **2001**, *34*, 1487–1492.
- (28) Kim, S. O.; Solak, H. H.; Stoykovich, M. P.; Ferrier, N. J.; de Pablo, J. J.; Nealey, P. F. *Nature* **2003**, *424*, 411–414.
- (29) Segalman, R. A.; Hexemer, A.; Kramer, E. J. *Macromolecules* **2003**, *36*, 6831–6839.
- (30) Cheng, J. Y.; Mayes, A. M.; Ross, C. A. *Nat. Mater.* **2004**, *3*, 823–828.
- (31) Stoykovich, M. P.; Muller, M.; Kim, S. O.; Solak, H. H.; Edwards, E. W.; De Pablo, J. J.; Nealey, P. F. *Science* **2005**, *308*, 1442–1446.
- (32) Cheng, J. Y.; Rettner, C. T.; Sanders, D. P.; Kim, H. C.; Hinsberg, W. D. *Adv. Mater.* **2008**, *20*, 3155–3158.
- (33) Wang, J. F.; Chen, Q. J.; Zhao, H.; Ming, T.; Wu, C. *J. Am. Chem. Soc.* **2009**, *131*, 16650–16651.
- (34) Zhang, M.; Wang, M. F.; He, S.; Qian, J. S.; Saffari, A.; Lee, A.; Kumar, S.; Hassan, Y.; Guenther, A.; Scholes, G.; Winnik, M. A. *Macromolecules* **2010**, *43*, 5066–5074.
- (35) Nie, Z.; Xu, S.; Seo, M.; Lewis, P. C.; Kumacheva, E. *J. Am. Chem. Soc.* **2005**, *127*, 8058–8063.
- (36) Xu, S. Q.; Nie, Z. H.; Seo, M.; Lewis, P.; Kumacheva, E.; Stone, H. A.; Garstecki, P.; Weibel, D. B.; Gitlin, I.; Whitesides, G. M. *Angew. Chem., Int. Ed.* **2005**, *44*, 724–728.
- (37) Seo, M.; Nie, Z.; Xu, S.; Mok, M.; Lewis, P. C.; Graham, R.; Kumacheva, E. *Langmuir* **2005**, *21*, 11614–11622.
- (38) Karnik, R.; Gu, F.; Basto, P.; Cannizzaro, C.; Dean, L.; Kyei-Manu, W.; Langer, R.; Forokhzad, O. C. *Nano Lett.* **2008**, *8*, 2906–2912.
- (39) Anderson, D. G.; Xu, Q. B.; Hashimoto, M.; Dang, T. T.; Hoare, Y.; Kohane, D. S.; Whitesides, G. M.; Langer, R. *Small* **2009**, *5*, 1575–1581.
- (40) Schabas, G.; Yusuf, H.; Moffitt, M. G.; Sinton, D. *Langmuir* **2008**, *24*, 637–643.
- (41) Schabas, G.; Wang, C.-W.; Oskooei, A.; Yusuf, H.; Moffitt, M. G.; Sinton, D. *Langmuir* **2008**, *24*, 10596–10603.
- (42) Wang, C.-W.; Oskooei, S. A. K.; Sinton, D.; Moffitt, M. G. *Langmuir* **2010**, *26*, 716–723.
- (43) Brown, L.; McArthur, S. L.; Wright, P. C.; Lewis, A.; Battaglia, G. *Lab Chip* **2010**, *10*, 1922–1928.
- (44) Jahn, A.; Vreeland, W. N.; Gaitan, M.; Locascio, L. E. *J. Am. Chem. Soc.* **2004**, *126*, 2674–2675.
- (45) Steinbacher, J. L.; Moy, R. W. Y.; Price, K. E.; Cummings, M. A.; Roychowdhury, C.; Buffy, J. J.; Olbricht, W. L.; Haaf, M.; McQuade, D. T. *J. Am. Chem. Soc.* **2006**, *128*, 9442–9447.
- (46) Malmstadt, N.; Nash, M. A.; Purnell, R. F.; Schmidt, J. J. *Nano Lett.* **2006**, *6*, 1961–1965.
- (47) Hautekeer, J.-P.; Varshney, S. K.; Fayt, R.; Jacobs, C.; Jerome, R.; Teyssie, P. *Macromolecules* **1990**, *23*, 3893–3898.
- (48) Zhong, X. F.; Varshney, S. K.; Eisenberg, A. *Macromolecules* **1992**, *25*, 7160–7167.
- (49) Yen, B. K. H.; Gunther, A.; Schmidt, M. A.; Jensen, K. F.; Bawendi, M. G. *Angew. Chem., Int. Ed.* **2005**, *44*, 5447–5451.

- (50) Oskooei, S. A. K.; Sinton, D. *Lab Chip* **2010**, *10*, 1732–1734.
- (51) Khan, S. A.; Gunther, A.; Schmidt, M. A.; Jensen, K. F. *Langmuir* **2004**, *20*, 8604–8611.
- (52) Gunther, A.; Jensen, K. F. *Lab Chip* **2006**, *6*, 1487–1503.
- (53) Due to discrepancies between actual and programmed (nominal) gas flow rates arising from the compressible nature of the gas and the high gas/liquid interfacial tension, actual gas flow rates were calculated from from image analysis of the flow and are reported in Supporting Information (Table S1).
- (54) Zaccone, A.; Gentili, D.; Wu, H.; Morbidelli, M. *J. Chem. Phys.* **2010**, *132*, 134903.
- (55) Zaccone, A.; Wu, H.; Gentili, D.; Morbidelli, M. *Phys. Rev. E* **2009**, *80*, 051404.
- (56) Melis, S.; Verduyn, M.; Storti, G.; Morbidelli, M.; Baldyga, J. *AIChE J.* **1999**, *45*, 1383–1393.
- (57) Zinchenko, A. Z.; Davis, R. H. *Phys. Fluids* **1995**, *7*, 2310–2327.
- (58) For calculating Pe , D_0 was estimated from off-chip dynamic light scattering data of similar sized PS-b-PAA micelles under the same temperature and solvent conditions.
- (59) Jusufi, A.; Likos, C. N.; Ballauff, M. *Colloid Poly. Sci.* **2004**, *282*, 910–917.
- (60) Zhang, L. E. A. *Macromolecules* **1996**, *29*, 8805–8815.
- (61) Grishchuk, A. A.; Estrin, Y. I. *Russ. J. Appl. Chem.* **2007**, *80*, 1940–1944.
- (62) Assuming that the internal densities and heights of spherical and nonspherical micelles are the same, the areal percentage of nonspherical micelles in TEM images should be roughly equivalent to their weight percentage relative to the entire micelle population.
- (63) Dormidontova, E. E. *Macromolecules* **1999**, *32*, 7630–7644.
- (64) Jones, J. L.; Marques, C. M.; Joanny, J.-F. *Macromolecules* **1995**, *28*, 136–142.
- (65) This mixing channel geometry run under similar conditions resulted in complete mixing of the liquid plug within 2 mm of the 10 mm mixing chamber (ref 41), or 0.5 s at the low flow rate. While this short channel length (and short duration) is sufficient to mix the reactants in the liquid plug, it is not sufficient to expose a significant volume of the liquid to the high shear hot spots in the corners of the liquid plug.
- (66) Reiter, G. *Phys. Rev. Lett.* **1992**, *68*, 75–78.